PRIMARY RESEARCH ARTICLE

WILEY Global Change Biology

Spatiotemporal pattern of gross primary productivity and its covariation with climate in China over the last thirty years

Yitong Yao[1] | Xuhui Wang[1] (iD) | Yue Li[1] | Tao Wang[2,3] (iD) | Miaogen Shen[2,3] | Mingyuan Du[4] | Honglin He[5] | Yingnian Li[6] | Weijun Luo[7] | Mingguo Ma[8] | Yaoming Ma[2,3] | Yanhong Tang[1] | Huimin Wang[5] | Xianzhou Zhang[5] | Yiping Zhang[9] | Liang Zhao[10] | Guangsheng Zhou[11] | Shilong Piao[1,2,3] (iD)

[1]Sino-French Institute for Earth System Science, College of Urban and Environmental Sciences, Peking University, Beijing, China

[2]Key Laboratory of Alpine Ecology and Biodiversity, Institute of Tibetan Plateau Research, Chinese Academy of Sciences, Beijing, China

[3]Center for Excellence in Tibetan Earth Science, Chinese Academy of Sciences, Beijing, China

[4]Institute for Agro-Environmental Sciences, National Agriculture and Food Research Organization, Tsukuba, Japan

[5]Key Laboratory of Ecosystem Network Observation and Modeling, Institute of Geographic Sciences and Natural Resources Research, Chinese Academy of Sciences, Beijing, China

[6]Key Laboratory of Adaptation and Evolution of Plateau Biota, Northwest Institute of Plateau Biology, Chinese Academy of Sciences, Xining, China

[7]State Key Laboratory of Environmental Geochemistry, Institute of Geochemistry, Chinese Academy of Sciences, Guiyang, China

[8]Cold and Arid Regions Remote Sensing Observation System Experiment Station, Cold and Arid Regions Environmental and Engineering Research Institute, Chinese Academy of Sciences, Lanzhou, China

[9]Key Laboratory of Tropical Forest Ecology, Xishuangbanna Tropical Botanical Garden, Chinese Academy of Sciences, Mengla, Yunnan, China

[10]Key Laboratory of Adaptation and Evolution of Plateau Biota, Haibei Alpine Meadow Ecosystem Research Station, Northwest Institute of Plateau Biology, Chinese Academy of Sciences, Xining, China

[11]State Key Laboratory of Vegetation and Environmental Change, Institute of Botany, Chinese Academy of Sciences, Beijing, China

Correspondence
Shilong Piao, Sino-French Institute for Earth System Science, College of Urban and Environmental Sciences, Peking University, Beijing, China.
Email: slpiao@pku.edu.cn

Abstract

The uncertainties of China's gross primary productivity (GPP) estimates by global data-oriented products and ecosystem models justify a development of high-resolution data-oriented GPP dataset over China. We applied a machine learning algorithm developing a new GPP dataset for China with 0.1° spatial resolution and monthly temporal frequency based on eddy flux measurements from 40 sites in China and surrounding countries, most of which have not been explored in previous global GPP datasets. According to our estimates, mean annual GPP over China is 6.62 ± 0.23 PgC/year during 1982–2015 with a clear gradient from southeast to northwest. The trend of GPP estimated by this study (0.020 ± 0.002 PgC/year^2 from 1982 to 2015) is almost two times of that estimated by the previous global dataset. The GPP increment is widely spread with 60% area showing significant increasing trend ($p < .05$), except for Inner Mongolia. Most ecosystem models overestimated the GPP magnitudes but underestimated the temporal trend of GPP. The monsoon affected eastern China, in particular the area surrounding Qinling Mountain, seems having larger contribution to interannual variability (IAV) of China's GPP than the semiarid northwestern China and Tibetan Plateau. At country scale, temperature is the dominant climatic driver for IAV of GPP. The area where IAV of GPP

dominated by temperature is about 42%, while precipitation and solar radiation dominate 31% and 27% respectively over semiarid area and cold-wet area. Such spatial pattern was generally consistent with global GPP dataset, except over the Tibetan Plateau and northeastern forests, but not captured by most ecosystem models, highlighting future research needs to improve the modeling of ecosystem response to climate variations.

KEYWORDS

China, climate change, eddy covariance, gross primary productivity, interannual variability, model tree ensemble

1 | INTRODUCTION

Gross primary productivity (GPP), describing photosynthetically carbon assimilation by vegetation per unit space and time (Monteith, 1972), is a pivotal flux that drives the terrestrial carbon cycle (Beer et al., 2010). As the largest carbon flux, minor change of GPP would significantly alter of ecosystem carbon balance, atmospheric CO_2 concentration and thus feedbacks to the climate (Ahlström et al., 2015; Ichii, Hashimoto, Nemani, & White, 2005; Piao, Ciais, et al., 2009). Therefore, quantifying GPP and its spatiotemporal variation is of priorities in carbon cycle studies.

Temporal variation of GPP can be analyzed from two aspects: decadal trend and interannual variability. While trend in GPP provides an integrative measure for impacts from all anthropogenic and natural forcings affecting GPP. Interannual variation of GPP reflects the year-to-year difference mainly driven by climate variations (Peng, Piao, Ciais et al., 2013; Weber et al., 2009), including the climate extremes (Zhao & Running, 2010; Zscheischler et al., 2014). Our understanding on global and regional interannual variations of GPP relies largely on ecosystem models and remains uncertain (Anav et al., 2015; Mao, Thornton, Shi, Zhao, & Post, 2012). Previous studies indicate that climatic drivers of GPP interannual variations include variations in temperature, precipitation, and solar radiation (Barman, Jain, & Liang, 2014; Richardson, Hollinger, Aber, Ollinger, & Braswell, 2007). For example, warmer temperature facilitates plant growth in cold regions, and thus can be regarded as one main reason for enhanced vegetation productivity over northern higher latitudes (Piao, Friedlingstein, Ciais, Viovy, & Demarty, 2007; Zhao & Running, 2010). Droughts controlled interannual variations of GPP over semiarid regions such as southwestern US (Mekonnen, Grant & Schwalm, 2016) and sub-Sahara Africa (Weber et al., 2009). Despite of potential role of solar radiation in regulating GPP over humid tropical or subtropical regions (e.g., Nemani et al., 2003), it has often been neglected in regional GPP analyses (e.g., Mekonnen, Grant, & Schwalm, 2016). As the response of GPP to climate variations depends on many factors such as baseline climate and vegetation types, regional studies on spatiotemporal variations of GPP are therefore helpful to reduce uncertainties in our understanding of the mechanisms driving the carbon cycle and to forecast GPP under expected future climate change. As a large country spanning from the tropics to the boreal zone and from humid to arid, and has almost all ecosystem types, China is an ideal region for such a study.

Accurate estimate of GPP over a region is not without challenges since direct GPP measurement is only applicable at leaf-level through photosynthesis measurements (Welp et al., 2011) or indirectly at ecosystem level with eddy covariance technique (Lee, 1998). Scaling-up these measurements are not straightforward (Yang, Shang, Guan, & Jiang, 2013). Machine learning algorithms have been developed to derive a global GPP dataset (Beer et al., 2010; Jung et al., 2011), which has been widely used as the benchmark to ecosystem models (e.g., Piao et al., 2013). The accuracy of the flux-based GPP dataset in part relies on the representativeness of the flux sites used (Beer et al., 2010). However, only nine flux sites in China have been used in the global dataset, which cannot well represent the diverse ecosystem types in China. The 0.5° spatial resolution is too coarse for regional scale study. With increasing number and representativeness of new flux sites and lengthening measurements, it is of interest to rebuild and examine the spatiotemporal variations of GPP in China, in order to further our understanding on the responses of carbon cycle to climate change.

In this study, we applied model tree ensemble (MTE) algorithm to develop a GPP dataset over China with 0.1° spatial resolution from 1982 to 2015 based on 40 flux sites, which represents almost all ecosystem types in China. Our main objectives are (1) developing high-resolution GPP products at regional scale based on updated flux site data; (2) identifying hotspots and subregional contributions to interannual variations in China's GPP; (3) understanding the dominant climatic driver to the interannual variations of GPP.

2 | MATERIALS AND METHODS

2.1 | Fluxnet eddy covariance data

Eddy covariance provides net ecosystem exchange (NEE) measurement (Baldocchi, 2008). The eddy covariance flux data used in this study were downloaded from ChinaFlux (www.chinaflux.org), Asia-Flux website (www.asiaflux.net), and global fluxnet database (www.fluxdata.org). The distribution of 40 flux sites is showed in Figure 1.
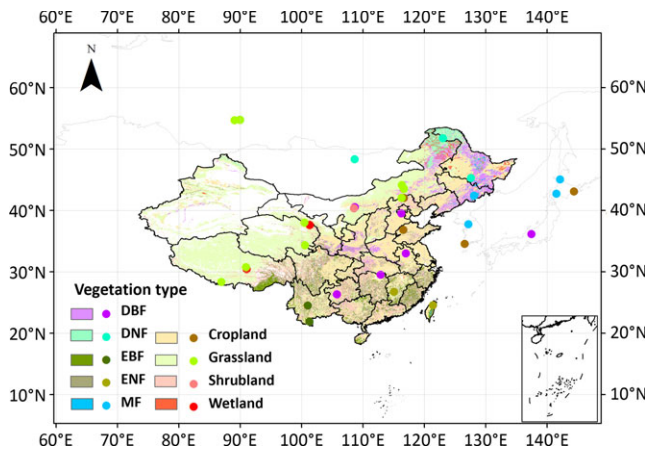
FIGURE 1 The distribution of flux sites used in this study. Land cover map was adapted from the vegetation distribution map of China

The specific characteristics of these 40 flux sites are listed in Table S1. The half-hourly flux measurements were gap filled and quality controlled using standardized procedures (Papale et al., 2006). GPP from eddy covariance NEE measurement is derived via Lasslop et al. (2010) method to separate GPP and terrestrial ecosystem respiration (TER). The half-hourly GPP data were first aggregated to daily scale, then averaged within a month. We collected 1,054 site-month flux data in total from 1999 to 2015.

2.2 | Climate and satellite data

We use the gridded reanalysis meteorological datasets for monthly mean air temperature, monthly precipitation sum, monthly shortwave radiation, which covered the period of 1982–2015 on a $0.1° \times 0.1°$ grid. This dataset was developed by Data Assimilation and Modeling Center for Tibetan Multi-spheres, Institute of Tibetan Plateau Research, Chinese Academy of Sciences (Chen et al., 2011; Yang, He, Tang, Qin, & Cheng, 2010), via merging Princeton reanalysis data, Global Energy and Water Cycle Experiment (GEWEX) Surface Radiation Budget (SRB) products, Global Land Data Assimilation System (GLDAS) data and ground-observed meteorological data from China Meteorological Administration (CMA). This reanalysis meteorological datasets have been evaluated against MODIS Land Surface Temperature (LST) products, CMA routine data, and GEWEX-SRB dataset (Chen, Yang, Zhou, Qin, & Guo, 2010; Chen et al., 2011; Yang et al., 2010). In general, the climate field from this high-resolution gridded dataset compares quite well with flux site measurements. The monthly temperature and radiation of the two datasets are well consistent. Monthly precipitation from the two datasets is also quite consistent, but with deviations for some sites in southern China. As the scale of spatial covariance in precipitation is finer than temperature and solar radiation, this seems a common issue, which has been reported in previous researches (Beer et al., 2010; Jung, Reichstein, & Bondeau, 2009). Meteorological datasets are much more uncertain with respect to precipitation compared to temperature (Zhao, Running, & Nemani, 2006).

During the identification of driving climate factors in process-based models, we use monthly climatic variables from the Climatic Research Unit National Centers for Environmental Prediction (CRUNCEP) dataset (New, Hulme, & Jones, 2000), including temperature, precipitation, and shortwave radiation.

Fraction of photosynthetically active radiation (FPAR) is used as a proxy for the photosynthetic activity characteristics of vegetation. The Global Inventory Modeling and Mapping Studies (GIMMS) FPAR was generated by an artificial neural network model and GIMMS Normalized Difference Vegetation Index (NDVI) dataset at 15-day time frequency and 1/12 degree resolution (Zhu et al., 2013, 2016). We first aggregated the original 15-day GIMMS FPAR data to monthly time step by maximum value composition (MVC) method (Holben, 1986), which is widely used in previous FPAR-based studies (Peng et al., 2012; Zhang et al., 2008), and then resampled the FPAR data to $0.1° \times 0.1°$ resolution by using nearest neighbor method.

2.3 | Vegetation distribution map

In this study, 1:1,000,000 China vegetation map was used (Editorial Board of Vegetation Map of China, Chinese Academy of Sciences, 2007). Five hundred and seventy-three vegetation types in the map were reclassified into nine categories, which are deciduous broadleaf forest (DBF), deciduous needle-leaf forest (DNF), evergreen broadleaf forest (EBF), evergreen needle-leaf forest (ENF), MF (mixed forest), cropland, grassland, shrubland, and wetland. The distribution of nine vegetation type is also showed in Figure 1 with lighter color than flux sites in the same class.

2.4 | GPP datasets

One data-driven global monthly GPP product (Jung et al., 2011) and monthly GPP simulations from nine TRENDY ("Trends in net land-atmosphere carbon exchange over the period 1980–2010") models: CLM4.5 (Oleson et al., 2013), ISAM (Jain, Meiyappan, Song, & House, 2013), JULES (Clark et al., 2011), LPJ (Sitch et al., 2003), LPX (Stocker, Spahni, & Joos, 2014), OCN (Zaehle & Friend, 2010), ORCHIDEE (Krinner et al., 2005), VEGAS (Zeng, Qian, Roedenbeck, & Heimann, 2005) and VISIT (Kato, Kinoshita, Ito, Kawamiya, & Yamagata, 2013), were used for comparison with GPP produced in this study. Jung et al. (2011) released a gridded monthly global GPP (hereafter, JUNG-GPP) by training MTE over 178 stations with climatic fields (temperature, precipitation, and potential radiation) and satellite-derived parameter (FPAR). The nine TRENDY models are forced by the global observed atmospheric CO_2 concentration and variable climate from CRU-NCEP dataset. We mainly evaluated model results from S3 simulation forced with time-variant CO_2, climate, and land use/cover. All monthly GPP from TRENDY models are first resampled to a uniform $0.5° \times 0.5°$ grid in unit of gC m^{-2} yr^{-1}. Both JUNG-GPP and TRENDY models provided GPP covering the time scope from 1982 to 2010. In discussion section, we used the same time span of GPP in this study for their comparison.

2.5 | GPP data reconstruction

In this study, the same MTE algorithm as Jung et al. (2009, 2010, 2011) was used to estimate gridded China GPP at $0.1° \times 0.1°$ resolution. The MTE was trained with monthly GPP as dependent variable and a series of explanatory variables listed in Table S2 as inputs. Then, the trained MTE was applied to whole China domain. GPP is estimated from the trained MTE based on climate variables and FPAR in each pixel.

2.6 | Trend and anomaly of GPP at grid and country scale

The temporal trend of total sum GPP weighted by area is calculated using linear least square regression method. The same method is also applied to annual GPP in each grid. The standard deviation of annual GPP over all studied years is calculated for each pixel like Mao et al. (2012) and Anav et al. (2015). GPP anomaly at country scale and grid scale were detrended from total annual GPP and annual GPP in each grid, respectively.

2.7 | Partition of interannual variability in China GPP

Partitioning of GPP interannual variability (IAV) to each grid is based on the definition of Equation (1) from Ahlström et al. (2015).

$$f_j = \frac{\sum_t \frac{x_{jt}|X_t|}{X_t}}{\sum_t |X_t|} \tag{1}$$

$$X_t = \sum_j x_{jt}. \tag{2}$$

Where x_{jt} is the GPP anomaly for region j at time t, and X_t is the China GPP total anomaly. f_j is the average relative anomaly x_{jt}/X_t for region j, weighted with the absolute China GPP total anomaly $|X_t|$. f_j ranges from -1 to 1. Higher positive f_j indicates IAV in the pixel varies in phase with integral IAV and larger local contribution toward China GPP IAV, while smaller or negative f_j represents the opposite.

2.8 | Characterizing relationships between GPP interannual variability and climatic factors

Besides annual GPP, we also detrended annual mean temperature, annual precipitation sum, and annual mean shortwave radiation time series in each grid. To derive the relative importance of these three climate factors in determining the GPP IAV, we used Lindeman-Merenda-Gold (LMG) method, which allows to differentiate the contribution of different correlated regressors in a multiple linear regression model from R software version 3.2.4 (R Core Team, 2016) with the package "relaimpo" (Grömping, 2006). The LMG method has been widely used in several previously published papers, some of them are in high-profile journals, e.g., Carvalhais et al. (2014), Fernández-Martínez et al. (2014), Musavi et al. (2017), etc. This metric is based on unweighted averages over sequential R^2s of each variable in all

permutation of available regressors to avoid regressors' order effects. And the total R^2 can be decomposed to non-negative components that sum to the total R^2 spontaneously. The explained power (R^2) of three climate factors was normalized to derive RGB combination to reflect climatic drivers of GPP IAV.

2.9 | The comparison map profile method

To detect spatial similarity and difference patterns, the comparison map profile (CMP) method, which is based on the absolute distance and cross-correlation coefficient through multispatial scales (Gaucherel, Alleaume, & Hely, 2008), is employed in this study. The absolute distance between moving window in two compared images is calculated as Equation (3), which provides absolute differences between them.

$$D = \text{abs}(\bar{x} - \bar{y}) \tag{3}$$

$\bar{x}$ and $\bar{y}$ are averages computed over two moving windows to be compared.

The cross-correlation (CC) coefficient is calculated as Equation (4), which suggests similar or contrasting directions in gradient (Gritti, Gaucherel, Crespo-Perez, & Chuine, 2013).

$$CC = \frac{1}{N^2} \sum_{i=1}^{N} \sum_{j=1}^{N} \frac{(x_{ij} - \bar{x}) \times (y_{ij} - \bar{y})}{\sigma_x \times \sigma_y} \tag{4}$$

$$\text{with } \sigma_x^2 = \frac{1}{N^2 - 1} \sum_{i=1}^{N} \sum_{j=1}^{N} (x_{ij} - \bar{x})^2 \tag{5}$$

x_{ij} and y_{ij} are the pixel value at row i and column j of two moving windows in two compared images, respectively. Each moving window covers N pixels. σ_x and σ_y are the standard deviation calculated over the two moving windows.

Low CC value indicates that similarity between two images is poor, and low D value indicates good agreement between them. Repeating these similarity index computation 20 times successively by increasing the window size from scale 1 (window size: 3×3 pixel) to scale 20 (window size: 41×41 pixel), the CMP method provides 20 monoscale similarity maps. All these monoscale maps can be integrated to one mean CMP map by averaging the similarity value over 20 monoscale in each pixel. This method enables the quantification of differences between images when changing spatial scales. GPP produced in this study is resampled to $0.5° \times 0.5°$ resolution to match the JUNG-GPP and TRENDY model mean during CMP comparison procedures. For detailed CMP method description, please refer to Gaucherel et al. (2008).

3 | RESULTS

3.1 | Spatiotemporal pattern of GPP over China

The high-resolution regional GPP dataset we developed in this study can successfully capture the spatiotemporal variations of GPP observed in the flux sites ($R^2 = 0.97$, $p < .01$). The robustness of the

dataset is still outstanding when compared to validation flux site data that were not put in training of MTE ($R^2 = 0.88$, $p < .01$; Figure 2a). Further, we assess the MTE performance in aspects of among-site variability, seasonal variations, and interannual anomalies (Fig. S1). MTE performs well in terms of all data, among-site variability, and seasonal variations (Fig. S1). According to the high-resolution regional GPP dataset, mean annual GPP during 1982–2015 over China is 6.62 ± 0.23 PgC/year. For the vegetated area, GPP shows a descendant gradient from southeast toward northwest (Figure 2b), with the highest value in the southeast (>2,000 gC m^{-2} yr^{-1}) and the lowest in northwest, Inner Mongolia and Tibetan Plateau (< 300 gC m^{-2} yr^{-1}). We also carry out the experiments that using only China flux sites or subset of flux measurements (to test the uncertainty associated with flux measurement period). These tests generate similar results (see Appendices S1 and S2).

Over the last thirty years, China's GPP increased from 6.31 PgC/year in 1982 to 6.94 PgC/year in 2015, with a significant temporal trend of 0.020 ± 0.002 PgC/year^2 (~0.32%/year, $p < .01$, Figure 3a). Meanwhile, annual temperature and precipitation also significantly increased at a rate of 0.04°C/year ($p < .01$) and 3.00 mm/year ($p < .01$), respectively (Figure 3b,c). Annual radiation presented large year-to-year variation with statistically insignificant trend at a rate of -0.03 W m^{-2} yr^{-1} ($p = .39$, Figure 3d). Interannual changes of annual GPP are highly correlated with annual mean temperature ($R = 0.86$, $p < .01$). Lower agreement occurred between annual GPP and annual radiation ($R = 0.36$, $p < .05$), followed by annual precipitation ($R = 0.30$, $p = .10$).

GPP trend in China presented a heterogeneous geographical pattern. Positive trends are widespread (89.5%), and almost 60% of the study region experienced a significant increase ($p < .05$). Magnitude of the trend in most area varies within the range of 0–4 gC m^{-2} yr^{-2}, in which is generally larger in the southeastern and the northeastern than that in the northwestern (Figure 4a). The largest increase in GPP (>6 gC m^{-2} yr^{-2}) occurred in densely forested area in Yunnan in the Southeast, southeast of Tibetan Plateau, Daxing'anling in the Northeast and Taiwan Island. Decreased trend of GPP was found for only 10.5% area (1.1% is significant, $p < .05$), and scattered mainly over semiarid grasslands in northern Inner Mongolia, magnitude of which can be larger than -4 gC m^{-2} yr^{-2} (Figure 4a). We further analyzed the standard deviation of annual

GPP over 1982–2015 and found that larger interannual variability occurred in forests in northeast area, Qinling Mountain and southeast of Tibetan Plateau (>100 gC m^{-2} yr^{-1}, Figure 4b), while the hinterland of Tibetan Plateau and Inner Mongolia are among the area with lower standard deviation (<50 gC m^{-2} yr^{-1}).

3.2 | Local and subregional contribution to GPP interannual variability over China

We applied Equation (1) (see Section 2; Ahlström et al., 2015) to analyze contribution of each pixel or each subregion to interannual variability of China's GPP (e.g., area-weighted sum of GPP over China) (Figure 4c). We found that, at pixel scale, interannual variability in most pixels is in phase with China's GPP (positive value in Figure 4c), except in northern Tibetan Plateau, Inner Mongolia, and western part of Northeast China. Therefore, although standard deviations of GPP seem largest in Daxing'anling in Northeast China (Figure 4b), the phase of the variability is different over this area. As the opposite phases canceling out themselves, the contribution to IAV of the northeastern pixels is not outstanding comparing to central China pixels where standard deviation of interannual variability is smaller. We also aggregate pixels into geographical subregions over China according to its physical geography (Piao, Fang, et al., 2009). As Qinling Mountain and surrounding area seem contributing most to IAV of China's GPP, we found that North China and South-west China contribute most to IAV of China's GPP (21% and 16%, respectively). The contributions of Northwestern China, Inner Mongolia, Qinghai-Tibetan area are less than 10%, indicating that the semiarid regions in China are not the dominant contributor to IAV of GPP.

3.3 | Spatial pattern of dominant climatic drivers to GPP interannual variation

We further examined the dominant climatic factor with decomposition of regression coefficients when regressing GPP against annual mean temperature, annual precipitation sum (precipitation acted as a proxy for soil moisture content approximately), and annual solar radiation. Overall, the dominant climate driver to IAV of GPP varies widely across the country. Temperature is the dominant factor for about 42% of the area, while precipitation and solar radiation-
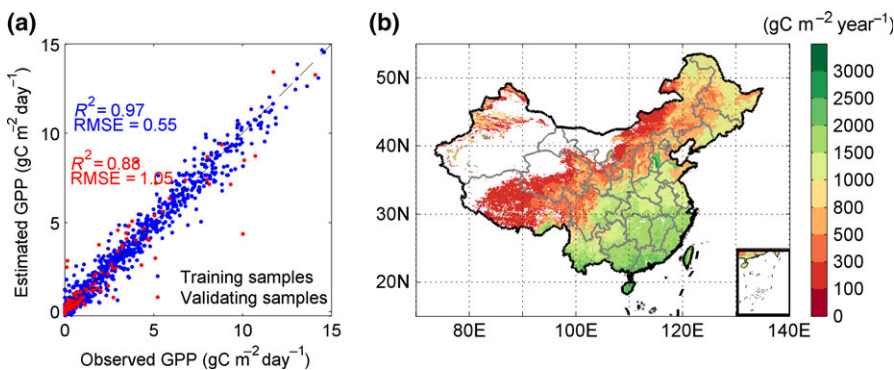
(a)

(b)

(gC m^{-2} year^{-1})

FIGURE 2 (a) The comparison between model tree ensemble (MTE) predicted gross primary productivity (GPP) and flux GPP observation. The performance of model tree was labeled. For training samples, $R^2 = 0.97$ and RMSE = 0.55 gC m^{-2} day^{-1}. For validating samples, $R^2 = 0.88$ and RMSE = 1.05 gC m^{-2} day^{-1}. (b) The spatial pattern of mean annual GPP in China during 1982–2015
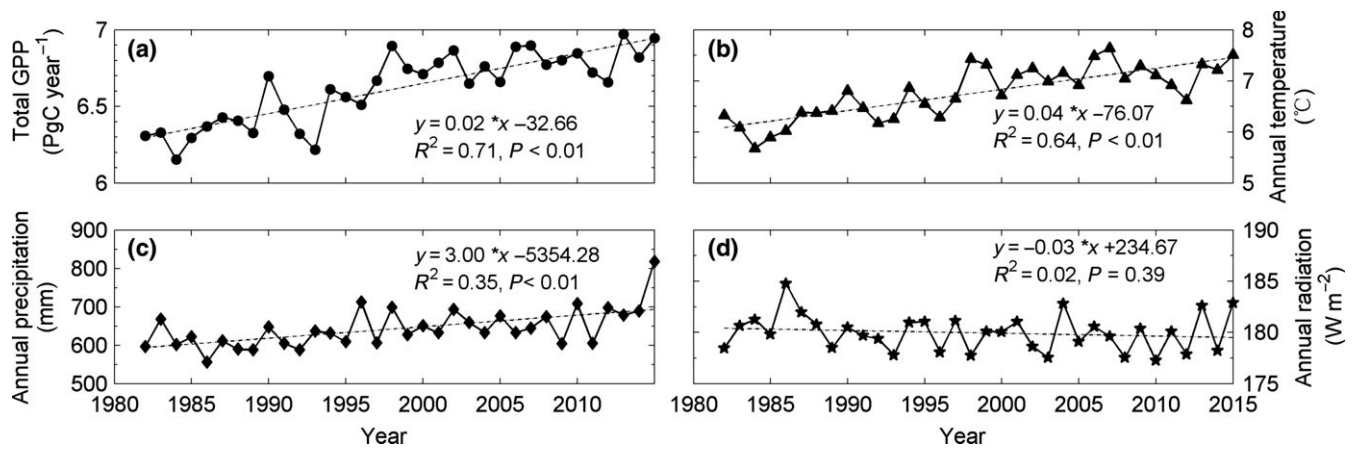
FIGURE 3 Interannual change in (a) annual total gross primary productivity (GPP), (b) annual mean temperature, (c) annual precipitation sum, and (d) annual radiation from 1982 to 2015
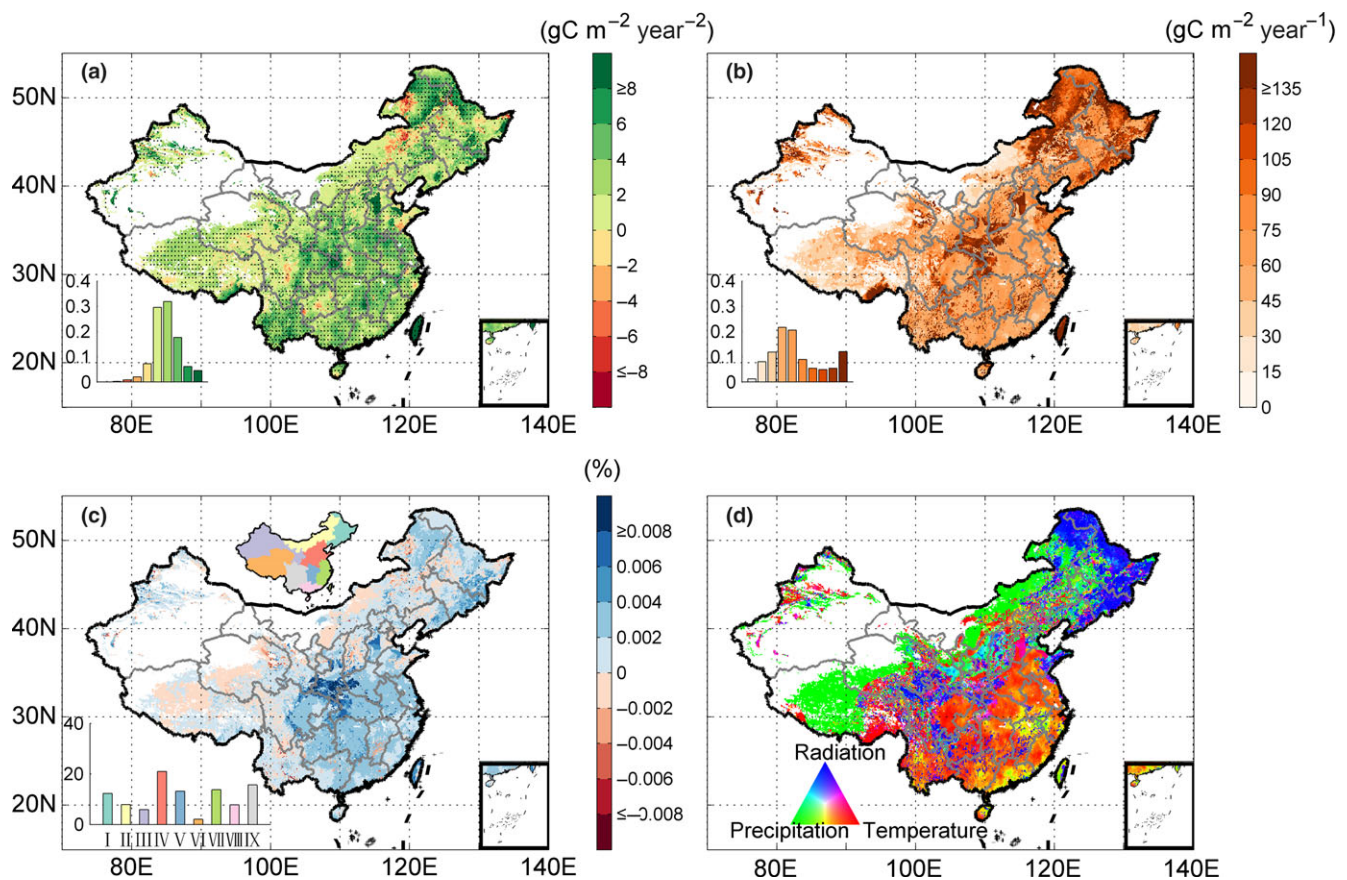

FIGURE 4 Spatial pattern of (a) temporal trend and (b) standard deviation of annual gross primary productivity (GPP) over 1982–2015, (c) local GPP contribution at pixel and subregional level to total GPP anomaly and (d) climate drivers for China GPP interannual variability. Black points mark pixels with significant linear trend of annual GPP during this time period in panel (a). The inset in panel (a) and (b) denotes the frequency distribution of linear trend and standard deviation for annual GPP. The top inset in panel (c) represents the geographical regionalization of China. The left inset in panel (c) indicates the contribution of nine subregion in China to total GPP anomaly. I: North-east China; II: Inner Mongolia, III: North-west China; IV: North China; V: Central China; VI: Qinghai-Tibetan Plateau; VII: Southeast China; VIII: South China, and IX: Southwest China

dominant IAV are about 31% and 27%, respectively (Figure 4d). Although the temperature-dominated area is only 10% more than that dominated by precipitation or by solar radiation, it distributed over North China, Southwest China, and eastern China (Figure 4d), where their contribution to IAV of China's GPP is almost 70% (Figure 4c). Thus, it is not surprising why at regional scale, IAV of

China's GPP is dominantly controlled by variations in temperature. IAV of GPP over most grassland area in Inner Mongolia and Tibetan Plateau is controlled by precipitation. It should be noted that even in the very cold central Tibetan, precipitation still outweighs temperature in driving the IAV of GPP (Figure 4d). In terms of that the contributions of GPP IAV in Inner Mongolia and Tibetan Plateau to GPP IAV at country scale are small and can cancel each other, relative importance of IAV in precipitation to GPP IAV at country scale is negligible. Solar radiation is the dominant climatic driver to IAV of GPP in northeastern border area and eastern edge of the Tibetan Plateau (Figure 4d). However, as these two areas have largely opposite phase in interannual variations (Figure 4c), we did not observe significant impact of solar radiation on IAV of China's GPP (Figure 2d).

4 | DISCUSSION

4.1 | GPP estimations by different global and regional datasets

Despite growing efforts in quantifying GPP, large uncertainties still exist. With higher resolution and better sampling for climate and vegetation types (Fig. S2), our GPP dataset can indeed reduce uncertainties due to interpolation and extrapolations, which are prevalent in the global GPP dataset. Although at the country scale GPP estimated by our product and JUNG-GPP remains similar (6.59 ± 0.23 PgC/year in our study and 6.35 ± 0.18 PgC/year in JUNG-GPP, 1982–2010), their spatial patterns differ. Compared with JUNG-GPP, our product has larger estimates of GPP for grassland over Tibetan plateau and Inner Mongolia, while much smaller GPP estimates over southeastern China (Figures 2b and S3a). As the data-oriented estimates are often served as the benchmark to process-based ecosystem models, we confront the TRENDY models (Sitch et al., 2015) to our dataset. The ensemble model mean seems

overestimating China's GPP by 19.1% (7.85 PgC/year), with inter-model range from 4.95 PgC/year in ISAM to 9.65 PgC/year in OCN (Figure 5a). Leaving out effects of human activity (Anav et al., 2015), natural disturbances (Liu et al., 2011), tropospheric ozone (Sitch, Cox, Collins, & Huntingford, 2007), and nutrient availability limitation (Goll et al., 2012; Piao et al., 2013) could have induced such biases. Uncertainty and differences in model structure and parameterization could also lead to such inconclusive estimation in simulating China GPP even to the same climate forcing (Sitch et al., 2008, 2015). In addition, there are some regional GPP estimates based on other models. For example, GPP estimation based on EC-LUE model (Eddy-Covariance Light Use Efficiency model, e.g., Li et al., 2013; Yuan et al., 2010) is more than 10% lower than that in this study albeit similar spatial gradient accompanied (Table 1), highlighting uncertainties related to model structure and parameters. Besides, two newly published researches generate rather high total amount of annual GPP in recent periods via multiple regression (Zhu et al., 2014) or Support Vector Regression (SVR, Ichii et al., 2017). Zhu et al. (2014) presents widespread greater GPP in majority areas of China except in Daxing'anling, north of Tibetan Plateau and southern area due to that climate-based potential GPP are considered. Asian GPP dataset from Ichii et al. (2017) derives higher China GPP mainly in Tibetan Plateau, Inner Mongolia, and part of southwest and southeast monsoon regions possibly due to their leaving out China flux sites like Tibetan Plateau and Inner Mongolia grassland flux sites as well as SVR-based prediction of GPP is greater than observation GPP to some extent when its value is less than 12 gC m^{-2} day^{-1} (Ichii et al., 2017).

Not only does the magnitude but also the spatial pattern of GPP is subject to large uncertainties. We further use spatial correlation to test the spatial consistency among different GPP datasets. The spatial correlation between global data-oriented dataset and regional data-oriented dataset in this study is quite high (Figure 5b), but the correlation strength between our dataset and model simulations may
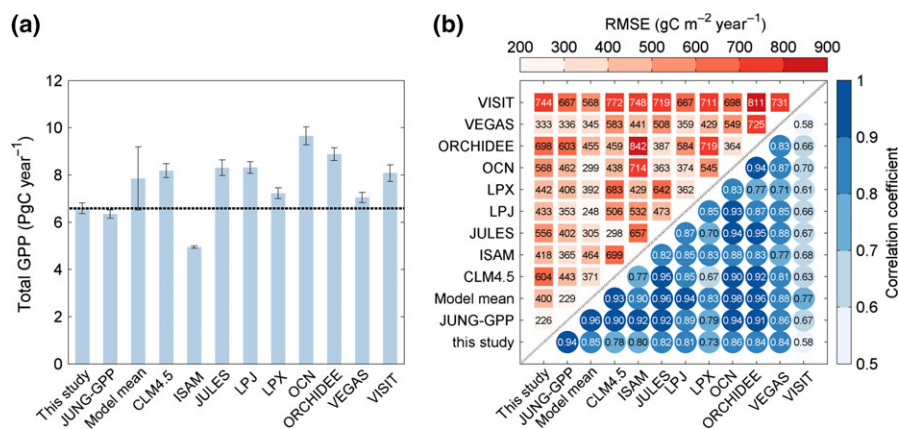

FIGURE 5 The (a) total gross primary productivity (GPP) weighted by area and (b) spatial correlation and RMSE among GPP in this study, JUNG-GPP and nine TRENDY models. The black dashed line in panel (a) indicates the corresponding mean total amount over 1982–2010 of GPP produced in this study. Error bar in panel (a) except "Model mean" indicates standard deviation of annual GPP over 1982–2010. Error bar in "Model mean" denotes the standard deviation, calculated as statistic of the 29 years mean for nine TRENDY models. In panel (b), the spatial correlation coefficients between any two datasets are highly significant ($p < .01$)

TABLE 1 Estimation of GPP in different terrestrial models over China

Model	GPP (PgC/year)	Study period	Reference
MOD17	5.53	2000–2014	Zhao, Heinsch, Nemani, and Running (2005)
EC-LUE	6.04	2000–2009	Li et al. (2013)
EC-LUE	5.55	2008–2009	Cai et al. (2014)
EC-LUE	5.38	2000–2009	Yuan et al. (2010)
Multiple regression	7.51	2001–2010	Zhu et al. (2014)
SVR	7.81	2000–2015	Ichii et al. (2017)
MTE	6.35	1982–2010	Jung et al. (2011)
MTE	6.62	1982–2015	This study

EC-LUE, Eddy-covariance light use efficiency; GPP, gross primary productivity; MTE, model tree ensemble; SVR, support vector regression.

vary quite a lot. The correlation coefficient varied from 0.58 to 0.86, indicating models differ in the simulated sensitivity of GPP to climate variations (Anav et al., 2015; Piao et al., 2013). The most outstanding difference is the overestimation of GPP in southern area by CLM4.5, LPJ, OCN, and ORCHIDEE (Fig. S3c,f,h,i), probably indicating the forest parameters used by these models cannot well represent the response of China's temperate forest to climate variations. In addition, these models still have limitations in representing the effects of human management (Anav et al., 2015; Guanter et al., 2014), which may greatly affect productivity estimation especially in intensively managed ecosystems such as croplands and forest plantations. Taking nitrogen availability into account could also bring substantial difference among models estimation. In terms of OCN and ORCHIDEE, whose disparity largely comes from whether nitrogen cycle is coupled or not, the former derives lower GPP value in southern area than the latter (Fig. S3 h,i), highlighting the need to incorporate full nutrient constraint on carbon fluxes (Wieder, Cleveland, Smith, & Todd-Brown, 2015).

The improvement of climate space sampling also has large influences on the magnitude and spatial distribution of GPP trends. Our dataset produced trend in China's GPP two times larger than that derived from the global dataset (0.012 PgC/year^2; Jung et al., 2011). When comparing our dataset and the JUNG-GPP dataset, we found that mean CMP distance and correlation comparison showed that the largest gradient consistency appears in Inner Mongolia (Mean correlation >0.4) and the largest discrepancy appeared in northeastern forests (Mean distance >3 gC m^{-2} yr^{-2}, Figure 6a,b). Disparity of GPP trend in northeastern forests could be related to following two reasons. The deciduous needle-leaf forest sites in northeastern China were not included in the construction process of global dataset (Jung et al., 2011), which cannot represent local responses to climate change. On the other hand, JUNG-GPP used monthly potential radiation (not vary over years) as a predictor, rather than monthly shortwave radiation that update monthly and yearly, which may affect accuracies of GPP in area sensitive to change in solar radiation (Figure 4d).

The trend produced in our study is also larger than the TRENDY model mean but within the range of the model ensemble (Fig. S4). Seven of the nine TRENDY models underestimate the trend in GPP, which may be related to several reasons. Firstly, Sun et al. (2014) found that global carbon cycle models underestimate photosynthetic responsiveness to atmospheric CO_2 change due to overestimation of mesophyll CO_2 transfer within leaves. Secondly, models without nitrogen constraint could have ignored the GPP trend increment induced by increasing nitrogen deposition in China (Tian et al., 2011), which may explain why the OCN with full nitrogen cycle produced two times the GPP trend than the similar model (ORCHIDEE) without nitrogen cycle (Fig. S4). Thirdly, the lack of explicit representation of agricultural management and crop physiology may lead to underestimate of GPP (Guanter et al., 2014) and the trend in cropland GPP resulted from green revolution, which may explain why many models do not show as large increasing trend in the North China Plain and Sichuan Basin as our dataset does (Figures 4a and S5). Finally, China has experienced unique afforestation processes over the past three decades (Piao, Fang, et al., 2009), models not considering this process (Sitch et al., 2015) would not be able to represent the increasing trend in large afforestation area such as the "Three North Program" (Duan et al., 2011) in Northeast, North and Northwest China (Figures 4a and S5) and Yangtze River Shelter afforestation program (Zhang, Song, Zhang, & Zhang, 2015) carried out in Yangtze River Basin (Figures 4a and S5). Indeed, CMP shows large distance between our dataset and TRENDY models over Inner Mongolia, northeastern China (Mean distance >3 gC m^{-2} yr^{-2}, Figure 6c) and mediate distance over Yangtze River Basin (Mean distance >1 gC m^{-2} yr^{-2}, Figure 6c). Gradient difference between trend in this study and model mean mainly concentrated in Tibetan Plateau (Mean correlation <−0.1, Figure 6d). Model mean shows large GPP increase in south of Tibet Plateau since six of nine TRENDY models identify temporal trend of > 6 gC m^{-2} yr^{-2} in this place (JULES, LPJ, LPX, OCN, ORCHIDEE, VISIT) while GPP in this study show weak increase of <4 gC m^{-2} yr^{-2} (Figures 4a and S5). Larger trend found in models could correspond to local enhanced precipitation, which implies overestimated sensitivity to precipitation variation for GPP simulated in models (Piao et al., 2013). Future efforts should focus on improving the model in response to climate variability and incorporating more missing processes to reduce systematic uncertainties (Keenan et al., 2012; Wang et al., 2014). Furthermore, we also compare GPP trends between TRENDY models and our data-driven product from the perspective of their radiation trend and FPAR trend difference (see Appendix S3).

4.2 | Interannual variability of GPP and its relationship with climate

Unlike the globe where semiarid regions contribute most to interannual variability (Ahlström et al., 2015), humid area in the eastern part of China seems dominating the interannual variability of GPP, with largest local contribution to total GPP anomaly was found in Qinling Mountain, which has not been previously identified. Interannual
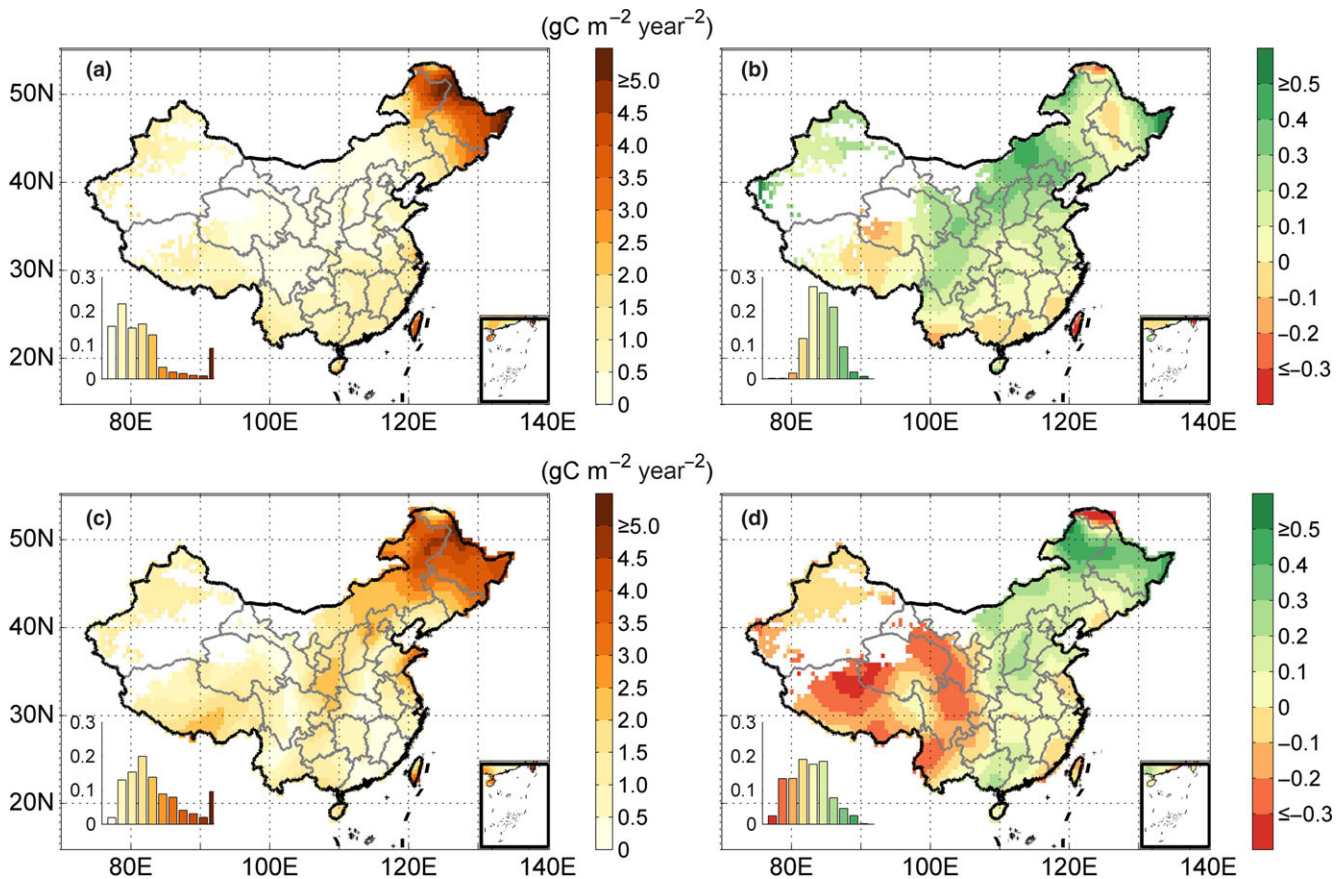
FIGURE 6 Comparison of annual gross primary productivity (GPP) linear trend in this study with (a, b) JUNG-GPP and (c, d) TRENDY model mean based on (a, c) absolute distance analysis and (b, d) cross-correlation analysis from Comparison Map Profile method. Panel (a) and (c) denote multiscale absolute distance map averaged over 20 monoscale distance maps. Panel (b) and (d) denote multiscale cross-correlation analysis through average of 4–20 monoscale correlation map (removing the overestimation of nonsignificant correlation in very small windows like 1–3 scale). The inset in four panels denotes the frequency distribution of multiscale average of absolute distance (a, c) and correlation (b, d), respectively

variability of photosynthetic activity potentially mirrors patterns of climate variability (Baker, Denning, & Stöckli, 2010). Climate over the eastern part of China is largely affected by East Asia monsoon, suggesting variability of monsoon is driving that of GPP. As temperature dominating the eastern part of China, it is not surprising that variability of China's GPP is more driven by temperature than by precipitation (Figure 3; He, Dong, Guo, & Dan, 2007), but, the climatic driver can diverse quite a lot spatially. In terms of forest areas having large annual precipitation (>1,000 mm), temperature increase could facilitate local forest growth without encountering water limitation (Piao et al., 2007). While in semiarid grasslands, moisture control on productivity in Inner Mongolia seems well consistent with field evidences (Bai et al., 2008) and modeling studies (Gerten et al., 2008; Peng, Piao, Shen, et al., 2013). Northeastern forests showed dominance of shortwave radiation on GPP variability. Kitamura et al. (2012) also found GPP IAV could be attributed to variations in shortwave radiation during foliated season in a forest site in Japan with similar latitudes, which seems supporting our findings. Future researches are still required to clarify why variability of GPP over regions such as Northeast China with low temperature and mediate precipitation is

driven mostly by solar radiation. Recently, Yang, Guan, Shen, Liang, and Jiang (2015) suggests that more radiation input would attenuate anaerobic soil condition induced by high soil moisture content. Although the hypothesis may seem promising, evidences are still lacking to support it at ecosystem level. We also noted that process-based ecosystem models present different dominant climatic driver to IAV of GPP except in semiarid Inner Mongolia (Fig. S6b–k). Five of nine TRENDY models show distinct temperature dominant effects in Tibetan Plateau (LPJ, LPX, OCN, VEGAS, VISIT), which are different from the dominance of precipitation identified by data-oriented products in this study (Figures 4d and S6f–h,j,k). Such discrepancies indicate that the ecosystem models still have a long way to go in order to correct the represent of carbon cycle response to climate variations. In addition, the dominant climatic drivers of modeled GPP in China differ a lot even among the models. For example, variations in precipitation dominate large area in CLM4.5 and JULES (Fig. S6c,e), but temperature seems to be the dominant driver in VEGAS (Fig. S6j). Such intermodel discrepancies reflect structural and parameterization differences in modeling GPP response to climate variable (Sitch et al., 2015). For TRENDY models, we also estimate the contribution of soil

moisture on GPP IAV using simulated soil moisture by TRENDY models (see Appendix S4).

4.3 | Uncertainties and future directions

Although data-oriented global GPP dataset has served as the benchmark for ecosystem models, previous studies recognized that the global dataset considerably underestimated the interannual variations of GPP (Jung et al., 2011; Piao et al., 2013), whether it is inherent in the methodology remains unclear (Jung et al., 2011). In our study, with the improvement of climate space sampling, which has filled the data gaps of typical ecosystems in China, and the variables representing interannual variations in solar radiations, we found our regional dataset indeed has distinctly larger interannual variability than the global dataset, which seems improving the precision of data-oriented GPP estimation. However, uncertainties remain in a few aspects. First of all, while effects of rising atmospheric CO_2 on plant growth (e.g., leaf area increment, Norby & Zak, 2011) are partially considered via FPAR, some physiological effects such as change in stomatal conductance and then water use efficiency are not explicitly represented in our approach. While the magnitude of CO_2 fertilization effects on GPP is still under debate (Gray et al., 2016), it will be interesting for future studies to test the machine learning algorithms against FACE experiments in order to quantify uncertainties in this aspect. Besides, other valuable information like human management and nature disturbance is also reflected by FPAR indirectly and spatially explicit distribution of these influential factors is required and could improve our estimation in the future. Moreover, previous studies show that IAV and trend in GPP derived from earlier version of JUNG-GPP could have been underestimated, since the trend and IAV of global GPP was much lower than that estimated by process-based models (e.g., Anav et al., 2013, 2015; Piao et al., 2013). Such issue was suspected to result from potential biases introduced by "spatial gradients extrapolation to temporal interannual gradients" (Jung et al., 2009; Piao et al., 2013; Reichstein et al., 2007), or leaving out some cumulative effects like soil moisture (Jung et al., 2007). However, latest version of machine learning methods derived carbon fluxes (GPP, TER and NEE) compared well with process-based model simulations (Jung et al., 2017). In addition, we found that, in our study over China, the magnitude of IAV and trend of GPP estimated by MTE algorithms compared well with the process-based ecosystem models (Figures 5 and S4). Therefore, at least for mostly temperate ecosystems in China, the MTE algorithm seems capable for trend analyses. The earlier version of JUNG-GPP trained MTE with La Thuile dataset, most stations of which had short measurement period. Thus, we suggest that improvement of the latest MTE products in representing trend and IAV of GPP seems indicating the importance of using longer term flux data in training MTE, which partially avoids extrapolating spatial gradients into temporal ones. Furthermore, the good performance of MTE on China seems suggesting that cumulative effects like soil moisture on GPP may be less important over temperate ecosystems than over the tropical forests, where deep soil reservoir (may >10 m) serves as

an important source of IAV of vegetation productivity (e.g., Gatti et al., 2014). Future studies based on increasing flux measurements over Amazon and Congo basins should further explore this issue of cumulative moisture effects on GPP variation.

REFERENCES

Ahlström, A., Raupach, M. R., Schurgers, G., Smith, B., Arneth, A., Jung, M., . . . Zeng, N. (2015). The dominant role of semi-arid ecosystems in the trend and variability of the land CO_2 sink. *Science*, 348, 895–899.

Anav, A., Friedlingstein, P., Beer, C., Ciais, P., Harper, A., Jones, C., . . . Zhao, M. (2015). Spatiotemporal patterns of terrestrial gross primary production: A review. *Reviews of Geophysics*, 53, 785–818.

Anav, A., Friedlingstein, P., Kidston, M., Bopp, L., Ciais, P., Cox, P., . . . Zhu, Z. (2013). Evaluating the land and ocean components of the global carbon cycle in the CMIP5 Earth System Models. *Journal of Climate*, 26, 6801–6843.

Bai, Y., Wu, J., Xing, Q., Pan, Q., Huang, J., Yang, D., & Han, X. (2008). Primary production and rain use efficiency across a precipitation gradient on the Mongolia plateau. *Ecology*, 89, 2140–2153.

Baker, I. T., Denning, A. S., & Stöckli, R. (2010). North American gross primary productivity: regional characterization and interannual variability. *Tellus B*, 62, 533–549.

Baldocchi, D. (2008). TURNER REVIEW No. 15'.Breathing'of the terrestrial biosphere: lessons learned from a global network of carbon dioxide flux measurement systems. *Australian Journal of Botany*, 56, 1–26.

Barman, R., Jain, A. K., & Liang, M. (2014). Climate-driven uncertainties in modeling terrestrial gross primary production: a site level to global-scale analysis. *Global Change Biology*, 20, 1394–1411.

Beer, C., Reichstein, M., Tomelleri, E., Ciais, P., Jung, M., Carvalhais, N., . . . Papale, D. (2010). Terrestrial gross carbon dioxide uptake: global distribution and covariation with climate. *Science*, 329, 834–838.

Cai, W., Yuan, W., Liang, S., Zhang, X., Dong, W., Xia, J., . . . Zhang, Q. (2014). Improved estimations of gross primary production using satellite-derived photosynthetically active radiation. *Journal of Geophysical Research: Biogeosciences*, 119, 110–123.

Carvalhais, N., Forkel, M., Khomik, M., Bellarby, J., Jung, M., Migliavacca, M., . . . Reichstein, M. (2014). Global covariation of carbon turnover times with climate in terrestrial ecosystems. *Nature*, 514, 213–217.

Chen, Y., Yang, K., He, J., Qin, J., Shi, J., Du, J., & He, Q. (2011). Improving land surface temperature modeling for dry land of China. *Journal of Geophysical Research: Atmospheres*, 116, D20104. https://doi.org/10.1029/2011JD015921

Chen, Y., Yang, K., Zhou, D., Qin, J., & Guo, X. (2010). Improving the Noah land surface model in arid regions with an appropriate parameterization of the thermal roughness length. *Journal of Hydrometeorology*, 11, 995–1006.

Clark, D. B., Mercado, L. M., Sitch, S., Jones, C. D., Gedney, N., Best, M. J., . . . Cox, P. M. (2011). The Joint UK Land Environment Simulator (JULES), model description–Part 2: carbon fluxes and vegetation dynamics. *Geoscientific Model Development*, 4, 701–722.

Duan, H., Yan, C., Tsunekawa, A., Song, X., Li, S., & Xie, J. (2011). Assessing vegetation dynamics in the Three-North Shelter Forest region of

China using AVHRR NDVI data. *Environmental Earth Sciences*, 64, 1011–1020.

Editorial Board of Vegetation Map of China, Chinese Academy of Sciences. (2007). *Vegetation Map of the People's Republic of China (1:1000000) (Digital version)*. Beijing, China: Geology Press.

Fernández-Martínez, M., Vicca, S., Janssens, I. A., Sardans, J., Luyssaert, S., Campioli, M., . . . Peñuelas, J. (2014). Nutrient availability as the key regulator of global forest carbon balance. *Nature Climate Change*, 4, 471–476.

Gatti, L. V., Gloor, M., Miller, J. B., Doughty, C. E., Malhi, Y., Domingues, L. G., . . . Lloyd, J. (2014). Drought sensitivity of Amazonian carbon balance revealed by atmospheric measurements. *Nature*, 506, 76–80.

Gaucherel, C., Alleaume, S., & Hely, C. (2008). The comparison map profile method: A strategy for multiscale comparison of quantitative and qualitative images. *Ieee Transactions on Geoscience and Remote Sensing*, 46, 2708–2719.

Gerten, D., Luo, Y., Le Maire, G., Parton, W. J., Keough, C., Weng, E., . . . Sowerby, A. (2008). Modelled effects of precipitation on ecosystem carbon and water dynamics in different climatic zones. *Global Change Biology*, 14, 2365–2379.

Goll, D. S., Brovkin, V., Parida, B. R., Reick, C. H., Kattge, J., Reich, P. B., . . . Niinemets, Ü. (2012). Nutrient limitation reduces land carbon uptake in simulations with a model of combined carbon, nitrogen and phosphorus cycling. *Biogeosciences*, 9, 3547–3569.

Gray, S. B., Dermody, O., Klein, S. P., Locke, A. M., McGrath, J. M., Paul, R. E., . . . Leakey, A. D. B. (2016). Intensifying drought eliminates the expected benefits of elevated carbon dioxide for soybean. *Nature Plants*, 2, 16132. https://doi.org/10.1038/nplants.2016.132

Gritti, E. S., Gaucherel, C., Crespo-Perez, M.-V., & Chuine, I. (2013). How can model comparison help improving species distribution models? *PloS one*, 8, e68823. https://doi.org/10.1371/journal.pone.0068823

Grömping, U. (2006). Relative importance for linear regression in R: the package relaimpo. *Journal of statistical software*, 17, 1–27.

Guanter, L., Zhang, Y., Jung, M., Joiner, J., Voigt, M., Berry, J. A., . . . Griffis, T. J. (2014). Global and time-resolved monitoring of crop photosynthesis with chlorophyll fluorescence. *Proceedings of the National Academy of Sciences*, 111, E1327–E1333.

He, Y., Dong, W., Guo, X., & Dan, L. (2007). Terrestrial growth in China and its relationship with climate based on the MODIS data. *Acta Ecologica Sinica*, 27, 5086–5092.

Holben, B. N. (1986). Characteristics of maximum-value composite images from temporal AVHRR data. *International journal of remote sensing*, 7, 1417–1434.

Ichii, K., Hashimoto, H., Nemani, R. R., & White, M. (2005). Modeling the interannual variability and trends in gross and net primary productivity of tropical forests from 1982 to 1999. *Global and Planetary Change*, 48, 274–286.

Ichii, K., Ueyama, M., Kondo, M., Saigusa, N., Kim, J., Alberto, M., . . . Zhao, F. (2017). New data-driven estimation of terrestrial CO_2 fluxes in Asia using a standardized database of eddy covariance measurements, remote sensing data, and support vector regression. *Journal of Geophysical Research: Biogeosciences*, 122, 767–795.

Jain, A. K., Meiyappan, P., Song, Y., & House, J. I. (2013). CO_2 emissions from land-use change affected more by nitrogen cycle, than by the choice of land-cover data. *Global Change Biology*, 19, 2893–2906.

Jung, M., Reichstein, M., & Bondeau, A. (2009). Towards global empirical upscaling of FLUXNET eddy covariance observations: validation of a model tree ensemble approach using a biosphere model. *Biogeosciences*, 6, 2001–2013.

Jung, M., Reichstein, M., Ciais, P., Seneviratne, S. I., Sheffield, J., Goulden, M. L., . . . Zhang, K. (2010). Recent decline in the global land evapotranspiration trend due to limited moisture supply. *Nature*, 467, 951–954.

Jung, M., Reichstein, M., Margolis, H. A., Cescatti, A., Richardson, A. D., Arain, M. A., . . . Williams, C. (2011). Global patterns of land-atmosphere fluxes of carbon dioxide, latent heat, and sensible heat derived from eddy covariance, satellite, and meteorological observations. *Journal of Geophysical Research: Biogeosciences*, 116, G00J07, https://doi.org/10.1029/2010jg001566

Jung, M., Reichstein, M., Schwalm, C. R., Huntingford, C., Sitch, S., Ahlström, A., . . . Zeng, N. (2017). Compensatory water effects link yearly global land CO_2 sink changes to temperature. *Nature*, 541, 516–520.

Jung, M., Vetter, M., Herold, M., Churkina, G., Reichstein, M., Zaehle, S., . . . Heimann, M. (2007) Uncertainties of modeling gross primary productivity over Europe: A systematic study on the effects of using different drivers and terrestrial biosphere models. *Global Biogeochemical Cycles*, 21, GB4021, https://doi.org/10.1029/2006gb002915

Kato, E., Kinoshita, T., Ito, A., Kawamiya, M., & Yamagata, Y. (2013). Evaluation of spatially explicit emission scenario of land-use change and biomass burning using a process-based biogeochemical model. *Journal of Land Use Science*, 8, 104–122.

Keenan, T., Baker, I., Barr, A., Ciais, P., Davis, K., Dietze, M., . . . Richardson, A. D. (2012). Terrestrial biosphere model performance for interannual variability of land-atmosphere CO_2 exchange. *Global Change Biology*, 18, 1971–1987.

Kitamura, K., Nakai, Y., Suzuki, S., Ohtani, Y., Yamanoi, K., & Sakamoto, T. (2012). Interannual variability of net ecosystem production for a broadleaf deciduous forest in Sapporo, northern Japan. *Journal of forest research*, 17, 323–332.

Krinner, G., Viovy, N., De Noblet-Ducoudré, N., Ogée, J., Polcher, J., Friedlingstein, P., . . . Prentice, I. C. (2005). A dynamic global vegetation model for studies of the coupled atmosphere-biosphere system. *Global Biogeochemical Cycles*, 19, GB1015, https://doi.org/10.1029/2003gb002199

Lasslop, G., Reichstein, M., Papale, D., Richardson, A. D., Arneth, A., Barr, A., . . . Wohlfahrt, G. (2010). Separation of net ecosystem exchange into assimilation and respiration using a light response curve approach: critical issues and global evaluation. *Global Change Biology*, 16, 187–208.

Lee, X. (1998). On micrometeorological observations of surface-air exchange over tall vegetation. *Agricultural and Forest Meteorology*, 91, 39–49.

Li, X., Liang, S., Yu, G., Yuan, W., Cheng, X., Xia, J., . . . Kato, T. (2013). Estimation of gross primary production over the terrestrial ecosystems in China. *Ecological Modelling*, 261, 80–92.

Liu, S., Bond-Lamberty, B., Hicke, J. A., Vargas, R., Zhao, S., Chen, J., . . . Oeding, J. (2011). Simulating the impacts of disturbances on forest carbon cycling in North America: Processes, data, models, and challenges. *Journal of Geophysical Research: Biogeosciences*, 116, G00K08, https://doi.org/10.1029/2010jg001585

Mao, J., Thornton, P. E., Shi, X., Zhao, M., & Post, W. M. (2012). Remote sensing evaluation of CLM4 GPP for the period 2000-09. *Journal of Climate*, 25, 5327–5342.

Mekonnen, Z. A., Grant, R. F., & Schwalm, C. (2016). Contrasting changes in gross primary productivity of different regions of North America as affected by warming in recent decades. *Agricultural and Forest Meteorology*, 218, 50–64.

Monteith, J. (1972). Solar radiation and productivity in tropical ecosystems. *Journal of applied ecology*, 9, 747–766.

Musavi, T., Migliavacca, M., Reichstein, M., Kattge, J., Wirth, C., Black, T. A., . . . Miguel, D. M. (2017). Stand age and species richness dampen interannual variation of ecosystem-level photosynthetic capacity. *Nature Ecology & Evolution*, 1, 0048. https://doi.org/10.1038/s41559-016-0048

Nemani, R. R., Keeling, C. D., Hashimoto, H., Jolly, W. M., Piper, S. C., Tucker, C. J., . . . Running, S. W. (2003). Climate-driven increases in global terrestrial net primary production from 1982 to 1999. *Science*, 300, 1560–1563.

New, M., Hulme, M., & Jones, P. (2000). Representing twentieth-century space–time climate variability. Part II: development of 1901–96

monthly grids of terrestrial surface climate. *Journal of climate*, 13, 2217–2238.

Norby, R. J., & Zak, D. R. (2011). Ecological lessons from free-air CO_2 enrichment (FACE) experiments. *Annual review of ecology, evolution, and systematics*, 42, 181–203.

Oleson, K. W., Lawrence, D. M., Bonan, G. B., Drewniak, B., Huang, M., Koven, C. D., . . . Yang, Z. (2013). *Technical Description of version 4.5 of the Community Land Model (CLM)*. Boulder, CO: Ncar Technical Note NCAR/TN-503+STR, National Center for Atmospheric Research.

Papale, D., Reichstein, M., Aubinet, M., Canfora, E., Bernhofer, C., Kutsch, W., . . . Yakir, D. (2006). Towards a standardized processing of Net Ecosystem Exchange measured with eddy covariance technique: algorithms and uncertainty estimation. *Biogeosciences*, 3, 571–583.

Peng, S., Piao, S., Ciais, P., Myneni, R. B., Chen, A., Chevallier, F., . . . Zeng, H. (2013). Asymmetric effects of daytime and night-time warming on Northern Hemisphere vegetation. *Nature*, 501, 88–92.

Peng, S., Piao, S., Shen, Z., Ciais, P., Sun, Z., Chen, S., . . . Chen, A. (2013). Precipitation amount, seasonality and frequency regulate carbon cycling of a semi-arid grassland ecosystem in Inner Mongolia, China: A modeling analysis. *Agricultural and Forest Meteorology*, 178, 46–55.

Peng, D., Zhang, B., Liu, L., Fang, H., Chen, D., Hu, Y., & Liu, L. (2012). Characteristics and drivers of global NDVI-based FPAR from 1982 to 2006. *Global Biogeochemical Cycles*, 26, GB3015, https://doi.org/10.1029/2011gb004060

Piao, S., Ciais, P., Friedlingstein, P., De Noblet-Ducoudré, N., Cadule, P., Viovy, N., & Wang, T. (2009) Spatiotemporal patterns of terrestrial carbon cycle during the 20th century. *Global Biogeochemical Cycles*, 23, GB4026, https://doi.org/10.1029/2008gb003339

Piao, S., Fang, J., Ciais, P., Peylin, P., Huang, Y., Sitch, S., & Wang, T. (2009). The carbon balance of terrestrial ecosystems in China. *Nature*, 458, 1009–1013.

Piao, S., Friedlingstein, P., Ciais, P., Viovy, N., & Demarty, J. (2007). Growing season extension and its impact on terrestrial carbon cycle in the Northern Hemisphere over the past 2 decades. *Global Biogeochemical Cycles*, 21, GB3018, https://doi.org/10.1029/2006gb002888

Piao, S., Sitch, S., Ciais, P., Friedlingstein, P., Peylin, P., Wang, X., . . . Zeng, N. (2013). Evaluation of terrestrial carbon cycle models for their response to climate variability and to CO_2 trends. *Global Change Biology*, 19, 2117–2132.

R Core Team (2016) *R: A Language and Environment for Statistical Computing*. R Foundation for Statistical Computing, Vienna, Austria. URL https://www.R-project.org/.

Reichstein, M., Papale, D., Valentini, R., Aubinet, M., Bernhofer, C., Knohl, A., . . . Seufert, G. (2007). Determinants of terrestrial ecosystem carbon balance inferred from European eddy covariance flux sites. *Geophysical Research Letters*, 34, L01402. https://doi.org/10.1029/2006GL027880

Richardson, A. D., Hollinger, D. Y., Aber, J. D., Ollinger, S. V., & Braswell, B. H. (2007). Environmental variation is directly responsible for short-but not long-term variation in forest-atmosphere carbon exchange. *Global Change Biology*, 13, 788–803.

Sitch, S., Cox, P., Collins, W., & Huntingford, C. (2007). Indirect radiative forcing of climate change through ozone effects on the land-carbon sink. *Nature*, 448, 791–794.

Sitch, S., Friedlingstein, P., Gruber, N., Jones, S. D., Murray-Tortarolo, G., Ahlström, A., . . . Myneni, R. B. (2015). Recent trends and drivers of regional sources and sinks of carbon dioxide. *Biogeosciences*, 12, 653–679.

Sitch, S., Huntingford, C., Gedney, N., Levy, P. E., Lomas, M., Piao, S., . . . Woodward, F. I. (2008). Evaluation of the terrestrial carbon cycle, future plant geography and climate-carbon cycle feedbacks using five Dynamic Global Vegetation Models (DGVMs). *Global Change Biology*, 14, 2015–2039.

Sitch, S., Smith, B., Prentice, I. C., Arneth, A., Bondeau, A., Cramer, W., . . . Venevsky, S. (2003). Evaluation of ecosystem dynamics, plant geography and terrestrial carbon cycling in the LPJ dynamic global vegetation model. *Global Change Biology*, 9, 161–185.

Stocker, B., Spahni, R., & Joos, F. (2014). DYPTOP: a cost-efficient TOP-MODEL implementation to simulate sub-grid spatio-temporal dynamics of global wetlands and peatlands. *Geoscientific Model Development*, 7, 3089–3110.

Sun, Y., Gu, L., Dickinson, R. E., Norby, R. J., Pallardy, S. G., & Hoffman, F. M. (2014). Impact of mesophyll diffusion on estimated global land CO_2 fertilization. *Proceedings of the National Academy of Sciences*, 111, 15774–15779.

Tian, H., Melillo, J., Lu, C., Kicklighter, D., Liu, M., Ren, W., . . . Running, S. (2011) China's terrestrial carbon balance: contributions from multiple global change factors. *Global Biogeochemical Cycles*, 25, GB1007, https://doi.org/10.1029/2010gb003838

Wang, X., Piao, S., Ciais, P., Friedlingstein, P., Myneni, R. B., Cox, P., . . . Chen, A. (2014). A two-fold increase of carbon cycle sensitivity to tropical temperature variations. *Nature*, 506, 212–215.

Weber, U., Jung, M., Reichstein, M., Beer, C., Braakhekke, M. C., Lehsten, V., . . . Rödenbeck, C. (2009). The interannual variability of Africa's ecosystem productivity: a multi-model analysis. *Biogeosciences*, 6, 285–295.

Welp, L. R., Keeling, R. F., Meijer, H. A., Bollenbacher, A. F., Piper, S. C., Yoshimura, K., . . . Wahlen, M. (2011). Interannual variability in the oxygen isotopes of atmospheric CO_2 driven by El Nino. *Nature*, 477, 579–582.

Wieder, W. R., Cleveland, C. C., Smith, W. K., & Todd-Brown, K. (2015). Future productivity and carbon storage limited by terrestrial nutrient availability. *Nature Geoscience*, 8, 441–444.

Yang, Y., Guan, H., Shen, M., Liang, W., & Jiang, L. (2015). Changes in autumn vegetation dormancy onset date and the climate controls across temperate ecosystems in China from 1982 to 2010. *Global Change Biology*, 21, 652–665.

Yang, K., He, J., Tang, W., Qin, J., & Cheng, C. C. (2010). On downward shortwave and longwave radiations over high altitude regions: Observation and modeling in the Tibetan Plateau. *Agricultural and Forest Meteorology*, 150, 38–46.

Yang, Y., Shang, S., Guan, H., & Jiang, L. (2013). A novel algorithm to assess gross primary production for terrestrial ecosystems from MODIS imagery. *Journal of Geophysical Research: Biogeosciences*, 118, 590–605.

Yuan, W., Liu, S., Yu, G., Bonnefond, J., Chen, J., Davis, K., . . . Verma, S. B. (2010). Global estimates of evapotranspiration and gross primary production based on MODIS and global meteorology data. *Remote Sensing of Environment*, 114, 1416–1431.

Zaehle, S., & Friend, A. (2010). Carbon and nitrogen cycle dynamics in the O-CN land surface model: 1. Model description, site-scale evaluation, and sensitivity to parameter estimates. *Global Biogeochemical Cycles*, 24, GB1005, https://doi.org/10.1029/2009gb003521

Zeng, N., Qian, H., Roedenbeck, C., & Heimann, M. (2005). Impact of 1998–2002 midlatitude drought and warming on terrestrial ecosystem and the global carbon cycle. *Geophysical Research Letters*, 32, L22709. https://doi.org/10.1029/2005GL024607

Zhang, K., Kimball, J. S., Hogg, E. H., Zhao, M., Oechel, W. C., Cassano, J. J., & Running, S. W. (2008). Satellite-based model detection of recent climate-driven changes in northern high-latitude vegetation productivity. *Journal of Geophysical Research: Biogeosciences*, 113, G03033. https://doi.org/10.1029/2007JG000621

Zhang, K., Song, C., Zhang, Y., & Zhang, Q. (2015). Natural disasters and economic development drive forest dynamics and transition in China. *Forest Policy and Economics*, 76, 56–64. https://doi.org/10.1016/j.forpol.2015.08.010

Zhao, M., Heinsch, F. A., Nemani, R. R., & Running, S. W. (2005). Improvements of the MODIS terrestrial gross and net primary production global data set. *Remote Sensing of Environment*, 95, 164–176.

Zhao, M., & Running, S. W. (2010). Drought-induced reduction in global terrestrial net primary production from 2000 through 2009. *Science*, *329*, 940–943.

Zhao, M., Running, S. W., & Nemani, R. R. (2006). Sensitivity of Moderate Resolution Imaging Spectroradiometer (MODIS) terrestrial primary production to the accuracy of meteorological reanalyses. *Journal of Geophysical Research: Biogeosciences*, *111*, G01002. https://doi.org/10/1029/2004JG000004

Zhu, X., Yu, G., He, H. L., Wang, Q., Chen, Z., Gao, Y., ... Sun, X. (2014). Geographical statistical assessments of carbon fluxes in terrestrial ecosystems of China: Results from upscaling network observations. *Global and Planetary Change*, *118*, 52–61.

Zhu, Z., Bi, J., Pan, Y., Ganguly, S., Anav, A., Xu, L., ... Myneni, R. B. (2013). Global data sets of vegetation leaf area index (LAI) 3g and Fraction of Photosynthetically Active Radiation (FPAR) 3g derived from Global Inventory Modeling and Mapping Studies (GIMMS) Normalized Difference Vegetation Index (NDVI3g) for the period 1981 to 2011. *Remote Sensing*, *5*, 927–948.

Zhu, Z., Piao, S., Myneni, R. B., Huang, M., Zeng, Z., Canadell, J. G., ... Zeng, N. (2016). Greening of the earth and its drivers. *Nature Climate Change*, *6*, 791–795.

Zscheischler, J., Mahecha, M. D., Von Buttlar, J., Harmeling, S., Jung, M., Rammig, A., ... Reichstein, M. (2014). A few extreme events dominate global interannual variability in gross primary production. *Environmental Research Letters*, *9*, 035001. https://doi.org/10.1088/1748-9326/9/3/035001

SUPPORTING INFORMATION

Additional Supporting Information may be found online in the supporting information tab for this article.

How to cite this article: Yao Y, Wang X, Li Y, et al. Spatiotemporal pattern of gross primary productivity and its covariation with climate in China over the last thirty years. *Glob Change Biol*. 2018;24:184–196. https://doi.org/10.1111/gcb.13830